RESEARCH ARTICLE

Multi-method characterization of sandstone pore size distribution heterogeneity and its influence on porosity and permeability variation

Junjian ZHANG[1], Fangkai QUAN (✉)[2,3], Hui ZHANG (✉)[1,4], Yinchuan SHAO[5], Yanning HAN[5], Yuqiang YANG[5], Xiangchun CHANG[1], Xiaoyang ZHANG[1]

1 College of Earth Sciences & Engineering, Shandong University of Science and Technology, Qingdao 266590, China
2 Key Laboratory of Coalbed Methane Resource & Reservoir Formation Process (Ministry of Education),
China University of Mining and Technology, Xuzhou 221008, China
3 School of Safety Science and Engineering, Anhui University of Science and Technology, Huainan 232001, China
4 Geophysical Prospecting and Surveying Team of Shandong Bureau of Coal Geological, Jinan 250104, China
5 Shandong Engineering Research Center of Mine Gas Disaster Prevention, Qingdao 266427, China

Abstract Pore volume/surface area and size distribution heterogeneity are two important parameters of pore structures, which restrict the gas-water-oil migration process in sandstone reservoirs. The fractal theory has been proved to be one of the most effective methods to quantify pore distribution heterogeneity. However, the dynamic variation of porosity and permeability due to fractal characteristics has been rarely studied. In this paper, physical properties, mineral composition, and pore distribution of 18 groups of sandstone samples were analyzed using scanning electron microscope (SEM) and high-pressure mercury injection tests. Then, Sierpinski model, Menger model, thermodynamic model, and multi-fractal model were used to calculate the fractal dimension of the pore volume. Thus, the relationship between fractal dimension and porosity/permeability variation rate, and pore compressibility were studied. The results are as follows. 1) All samples can be divided into three types based on pore volume (0.9 $cm^3 \cdot g^{-1}$) and mercury removal efficiency (35%), i.e., Type A (< 0.9 $cm^3 \cdot g^{-1}$ and < 35%); Type B (> 0.9 $cm^3 \cdot g^{-1}$ and <35%); Type C (> 0.9 $cm^3 \cdot g^{-1}$ and > 35%). 2) Four fractal models had poor applicability in characterizing fractal characteristics of different sample types. The fractal dimension by the Sierpinski model had a good linear correlation with that of other models. Pores with smaller volumes dominated the overall pore distribution heterogeneity by multi-fractal dimension. The pore diameter between 200−1000 nm and larger than 1000 nm was the key pore size interval that determined the fractal characteristics. 3) With the increase of confining pressures, porosity and permeability decreased in the form of a power function. The compressibility coefficient of typical samples was 0.002−0.2 MPa^{-1}. The compressibility of Types A and B was significantly higher than that of Type C, indicating that the total pore volume was not the key factor affecting the pore compressibility. The correlation of compressibility coefficient/porosity variation rate with pore volume (total and different size pore volume), fractal value and mineral component were not significant. This indicates that these three factors comprehensively restricted pore compression.

Keywords tight sandstone, pore size distribution, fractal dimension, multi-fractal model, permeability-porosity

1 Introduction

Different from conventional reservoirs, tight sandstone reservoirs are characterized by lower abundance, porosity, permeability and well production (Zou et al., 2012; Wang et al., 2018; Liu et al., 2020). Its pore-throat structure is the main factor affecting reservoir productivity and permeability. Therefore, pore structure, including pore throat size, morphology, connectivity and heterogeneity, has become one of the most important factors to evaluate sandstone reservoirs (Hou et al., 2020; Hu et al., 2020).

Quantitative characterization of the pore-throat system can be divided into fluid injection and image analysis methods. High-pressure mercury injection (HPMI) and

low field nuclear magnetic resonance (LF-NMR) are representative methods of the fluid injection method, which have been used to characterize the pore-throat system of sandstone reservoirs (Wang et al., 2014; Lai et al., 2016; Mastalerz et al., 2017; Cai et al., 2018; Zhang et al., 2019a; Zhang et al., 2020a). According to the mercury volume variation in HPMI, mercury intrusive and withdrawal curves are obtained. Then, pore structure parameters (pore volume and specific surface area) are calculated. HPMI has the advantage of rapidly and accurately characterizing a pore-facture system without damage, and the testing principle of instruments and equipment is simple (Schmitt et al., 2013). However, this method will damage the pore structure (e.g., 3 nm) at a higher pressure (e.g., 400 MPa). Thus, it has limitations in characterizing smaller pores (less than 100 nm) (Shao et al., 2018; Zhang et al., 2019a). Compared with unconventional reservoirs such as shale and coal reservoirs (Li et al., 2019), smaller pores of conventional and tight sandstone are not developed. Therefore, the HPMI test has become the most common method to characterize the pore-throat system of sandstone reservoirs (Lai et al., 2016, 2018; Su et al., 2018; Zhu et al., 2018).

As one of the key parameters of the pore-throat structure, pore size distribution (PSD) heterogeneity also affects the dynamic variation of porosity and permeability (Yao and Liu, 2012; Qiao et al., 2022). Various literature shows that fractal theory has been used to quantitatively characterize PSD heterogeneity. The study of fractal theory using the HPMI test can be divided into three stages.

Firstly, fractal characteristics of seepage pores (with a diameter above 100 nm) are described using one single fractal model, and the relationship between fractal dimension and porosity, and permeability parameters is discussed. The Menger model was used to analyze 34 middle-high rank coal samples by Yao et al. (2009). The results show that the fractal dimension of the seepage pore had a linear negative correlation with permeability, and the fractal dimension varied in a U shape with the increase of coal rank. Cai et al. (2016) calculated the fractal dimension of middle-high rank coal samples using the thermodynamic model, and the fractal dimension and pore permeability equations were established. Currently, several single fractal models have been developed, including the Menger model (Friesen and Mikula, 1987; Pfeifer and Avnir, 1983), the Sierpinski model (Angulo et al., 1992) and a thermodynamic fractal model.

Secondly, the fractal dimension of different fractal models is calculated for the same sample, and the applicability of different fractal models to specific study areas and reservoir types is discussed (Li, 2010; Cai et al., 2011; Peng et al., 2017; Su et al., 2018; Lu et al., 2018). Peng et al. (2017) studied the PSD heterogeneity of coals and tight sandstone using different mercury intrusion fractal models, and the results show that there was a weak correlation among those fractal dimensions and that the applicability of different fractal models to different reservoir types was variable. Yu et al. (2018) and Lu et al. (2018) studied the applicability of different fractal models to PSD heterogeneity of low to middle-rank coal samples and concluded that the Menger model was not suitable for characterizing their PSD heterogeneity. Hu et al. (2020) studied the applicability of single-fractal models to tight sandstone in the Ordos Basin and concluded that the thermodynamic model was not suitable for calculating the fractal pore dimension in tight sandstone reservoirs. Zhang et al. (2022) reported that the thermodynamic model was applicable to quantitatively characterize the PSD heterogeneity of shale collected from this sampling area. In general, there are different preferential fractal models in different literature due to the limitations of sample types and experimental conditions.

Thirdly, some literature has shown that multi-fractal theories can clarify fine structure inside the reservoir by studying the fractal characteristics of different areas (Friesen and Mikula, 1987; Paz Ferreiro and Vidal Vázquez, 2010; Li et al., 2015; Qin et al., 2018). Then, multi-fractal dimensions can be calculated for the corrected HPMI data using the multi-fractal method. Based on HPMI data of high-pressure section corrected by liquid nitrogen tests, Li et al. (2015) studied PSD of deformed coal using a generalized dimension D_Q. The results show that each fractal dimension parameter was highly consistent with the specific surface area and volume distribution, verifying the applicability of the multifractal theory in characterizing coal reservoir heterogeneity (Yu et al., 2018; Liu et al., 2019). Although the multifractal theory has obvious advantages in detailed characterization, the geometric significance of pores corresponding to those multi-fractal parameters remains unclear (Hu et al., 2020; Zhang et al., 2020b).

Generally, the study on PSD heterogeneity using HPMI tests has gradually developed from single fractal models to multifractal models. The applicability of the fractal model is still the most important research content. In addition, the correlation between single fractal parameters and initial porosity, and permeability has been widely studied. During oil and gas drainage, reservoir porosity and permeability constantly vary as the reservoir pressure decreases. However, the correlation between different fractal parameters and dynamic variation of porosity and permeability has been rarely studied.

In this paper, 18 sandstone samples were collected from the study area for HPMI testing, mineral composition and thin-slicing analysis. The Sierpinski model, the Menger model, the thermodynamic model and the multi-fractal model were used to comprehensively calculate the fractal dimension of pore volumes. In addition, the effects of porosity and permeability variation on confining pressures were studied. Thus, the relationship between fractal dimension and porosity/permeability variation rate as

well as the pore compressibility were studied.

2 Study area and experimental methods

2.1 Sample preparation

The sampling area is located in the Jinlong area of northwest Junggar Basin, China. The main structure is a wide and gently sloping meganose structure dipping to the southeast. The north wing of the bulge is gentle, transiting from the slope to the Mahu Depression (He et al., 2020). The Permian stratum is the main target area, and its main structure is a southeast-dipping monocline (Gao, 2016). Eighteen fresh sandstone samples were collected from Well A. Distribution and parameters of the samples are shown in Table 1.

The collected samples were packaged and immediately shipped to the laboratory for pre-testing and analysis. Scanning electron microscope (SEM) analysis was performed on a small amount of each sample and then HPMI tests were conducted to quantitatively study pore volume, specific surface area and PSD. The analytical protocol is as follows.

All samples were ground to about 60−80 mesh, and X-ray diffraction (XRD) analysis of the whole rock mineral was carried out using an Ultima IV instrument by Sinopec East China Branch. Then, HPMI analysis was conducted on the samples using an IV9500 mercury intrusion instrument. Twenty pressure points were measured for each sample with an analysis time of 5 s per point. The working pressure of the mercury intrusion analyses ranged from 0 to 30 MPa. The distribution and specific surface area of pores were determined using the Brunauer-Emmett-Teller (BET) model (Schmitt et al., 2013; Zou et al., 2013).

A total of 8 cylinders with the same diameter×length (25 mm×50 mm) were prepared for overburden permeability and porosity tests. The different permeability was measured by pressure-sensitive testing using an AP-608 overpressure posmometer. The experimental gas was made of high-purity helium, and the experimental method was based on the non-steady-state pressure drop method. During the measurement process, the gas pressure difference between the two ends of the core holder was set as 0.7 MPa to form an initial decay pressure pulse. Based on the instrument, the pressure decay data were automatically tested and the pulse decay permeability values at different confine pressure and pore pressure points were calculated. The effective stress was continuously increased to 50 MPa by changing the confining pressure (the gas pressure was maintained at 1 MPa) (Zhang et al., 2019b). In addition, each pressure point was tested for 30 min to eliminate the effects of pressurization time and total volume change, and the two pressure points were maintained at an interval of 30 s (Fig. 1).

Table 1 Basic information of sandstone samples

| Sample No.	Depth/m	Porosity/%	Permeability/mD	Mercury removal efficiency/%	Mineral composition/%		
					Clay content	Quartz	Feldspar
1	3945.18	7.1	0.816	25.1	2.6	31.68	31.68
2	4068.46	4.3	0.14	29.92	4.7	41.18	30.59
3		7.3	0.036	32.71	5.71	59.55	34.74
4	3959.12	8.1	0.363	31.26			
5	3970.47	8.3	0.756	31.26	3.08	16.85	20.02
6	4069.78	11.9	0.935	20.25	1.55	57.63	27.61
7		11.5	1.26	21.68			
8	3969.43	10.9	0.729	25.86			
9	3972.21	13.7	36.4	26.11			
10	4075.36	11.5	0.095	30.87			
11	4093.79	9.5	0.546	31.47	4.15	59.17	31.95
12	4076.19	9	0.078	31.95	4.96	68.07	26.97
13	3971.69	11.5	5.17	35.18			
14	4012.94	13.3	2.02	36.06			
15		9	0.171	36.44	4.38	62.56	24.8
16	4010.68	12.6	1.62	37.95	1.87	11.36	25.82
17	3955.52	14.2	9.67	39.32	0.46	5.13	8.21
18	3971	11.1	0.368	41.35			
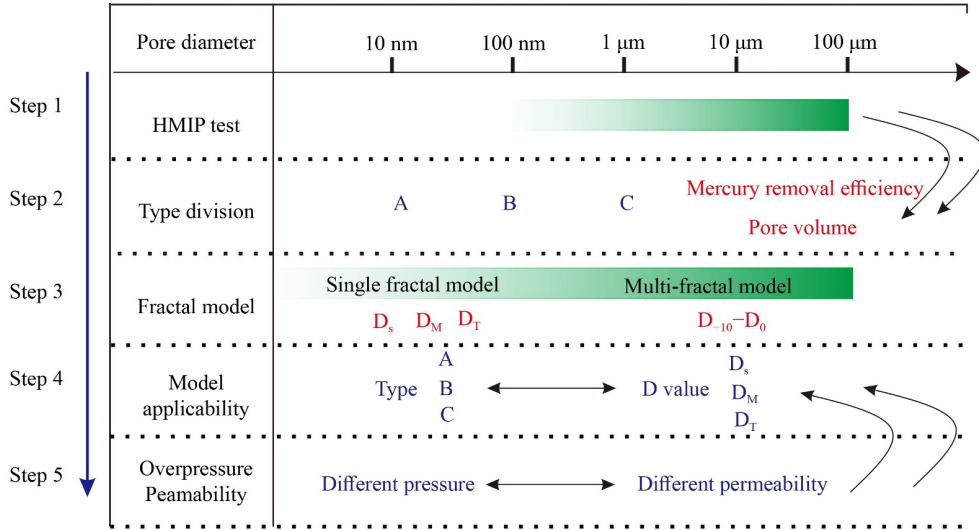
Fig. 1 Experimental methods and calculation theories.

2.2 Theoretical framework

2.2.1 Quantitative characterization of pore size distribution heterogeneity

In this paper, four representative fractal models were discussed, i.e., Menger, Sierpinski, thermodynamic, and multi-fractal models.

The Menger model. The Menger model, the most widely used single fractal model, is expressed as (Zhang et al., 2022)

$$\lg (dV_{obs}/dP) \propto (D-4)\lg P, \tag{1}$$

where D is the fractal dimension, dimensionless; P is injection pressure, MPa; V is total injection volume, cm$^3 \cdot$g^{-1}.

The Sierpinski model. A detailed derivation of the Sierpinski model can be found in Hu et al. (2020). The expression is

$$\ln V = (3-D)\ln (P - P_t) + \ln \alpha, \tag{2}$$

where V is mercury amount injected into among sample, mL; P is injecting pressure, MPa; P_t is the threshold pressure, MPa; D is the fractal dimension; α is a constant.

The thermodynamic model. With the injection pressure increasing, the volume of mercury gradually increases, resulting in an increased surface energy of the system. The mercury increment and pore surface energy conforms to

$$dW = -Pdv = -r_L \cos\theta dS. \tag{3}$$

Thus, the relationship between increments of mercury pressed into the pores Q_n and the surface energy W_n is written as

$$\ln W_n = \ln Q_n + C. \tag{4}$$

Eq. (4) is rewritten as

$$\ln\left(W_n/r_n^2\right) = D\ln\left(V_n^{1/3}/r_n\right) + C, \tag{5}$$

where V_n is the pore volume, mL/g; r_n is the pore radius, m; D is the surface fractal dimension (the slope of Eq. (9)).

The multi-fractal model. Detailed model derivation can be found in Zhang et al. (2020a). The multifractal features of one sample can be divided into fractal and singular spectra. $A \sim f(a)$ is a set of basic descriptions of the local features of multifractals, i.e., multifractal spectra. The other set $q \sim D(q)$ is introduced from the perspective of information theory and called the generalized fractal dimension. It should be noted that these two sets of parameters have a good linear relationship. Thus, only one type of parameters was used to describe the multifractal feature of the same sample.

2.2.2 Pore compressibility coefficient derivation

To study the effect of effective stress on permeability, a dimensionless parameter-porosity and permeability variation rate was introduced to describe permeability sensitivity, expressed as

$$D_k = \frac{k_0 - k_i}{k_0} \times 100\%, \tag{6}$$

where D_k is porosity and permeability variation rate; k_0 is initial permeability, mD; k_i is permeability under specific confining pressure, mD.

Seidle derived a classical formula involving permeability and stress using DP-P experimental tests:

$$k = k_0 e^{-3c_f(\sigma - \sigma_0)}, \tag{7}$$

where C_f is pore compressibility coefficient under horizontal effective stress variation, MPa^{-1}; k is

permeability after horizontal stress varies to σ MPa, mD; k_0 is the initial permeability, mD.

Based on the logarithmic operation of Eq. (2), the calculation method of C_f using the DP-P test can be obtained through

$$C_f = \frac{-\ln(k/k_0)}{3(\sigma - \sigma_0)}. \tag{8}$$

3 Results and discussion

3.1 Sample classification using mercury injection parameters

The mineralogical composition of all sandstone samples is illustrated in Table 1. Table 1 shows that quartz content ranged from 5.13% to 68.07%, with an average content of 41.32%. Clay mineral content ranged from 0.46% to 5.76%, with an average content of 3.35%. Carbonate mineral content ranged from 2.35% to 23.53%, with an average content of 10.42%. Porosity and permeability ranged from 4.3%−14.2% and 0.04%−9.67%, respectively. The sample type was determined using total pore volume and mercury removal efficiency using HPMI tests (Fig. 2). All sandstone samples were classified into three types, i.e., Types A, B, and C. Type A was characterized by lower total injection volume (< 0.9 cm³·g⁻¹) and lower mercury removal efficiency (< 33%). Type B was characterized by higher total injection volume (> 0.9 cm³·g⁻¹)
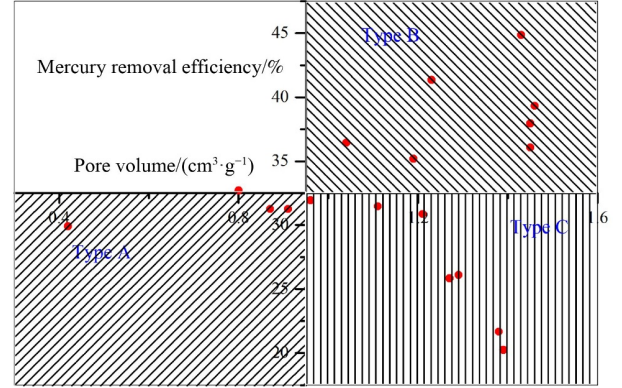

Fig. 2 Sample classification results using high-pressure mercury injection test parameters.

and lower mercury removal efficiency (< 33%). Type C was characterized by higher total injection volume (> 0.9 cm³·g⁻¹) and higher mercury removal efficiency (> 33%).

Figure 3 shows that pore morphology and type varied greatly in different sandstone samples. Through SEM and microscopic thin section observation, three types of pores were mainly developed in those sandstone samples, i.e., intergranular pores, dissolution pores and intergranular pores (Fig. 2). A small number of micro-fractures were also developed, mainly in gravel, with short extension distance and limited improvement on the sandstone permeability (Fig. 3(c)). Intergranular pores originated from remnants of primary pores, which were associated with secondary enlargement of quartz or clay inclusion
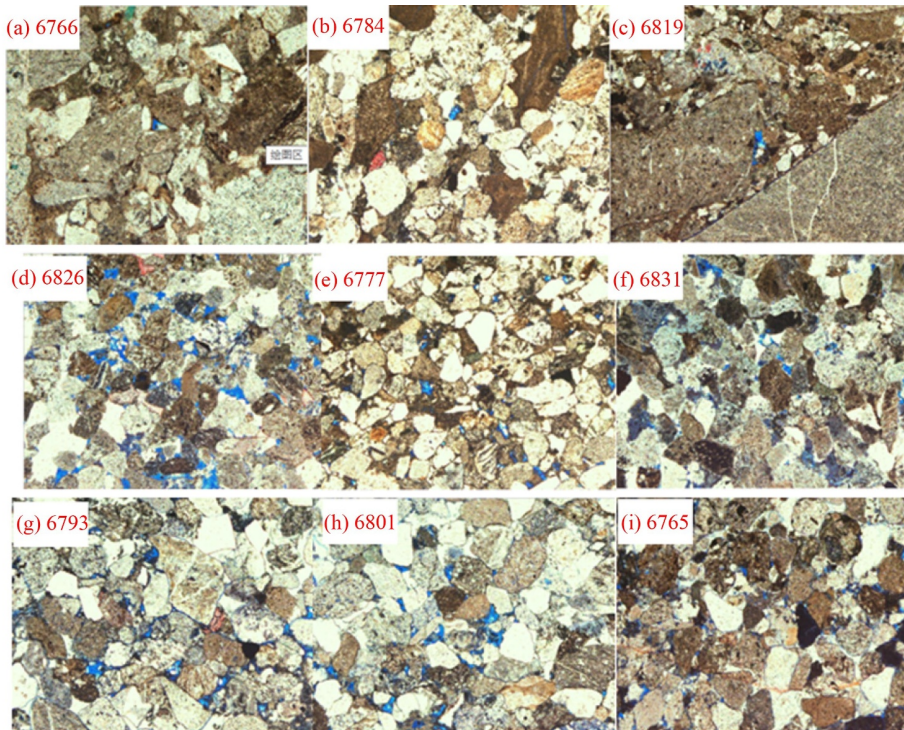

Fig. 3 Pore classification of typical samples using a founding slice.

(Figs. 3(a) and 3(b)). The number of intergranular pores was small and dispersed, which were usually connected by curved flake throat or micro-cracks between particle contact surfaces (Figs. 3(d) and 3(f)). Dissolution pores were caused by the dissolution of unstable components (mainly feldspar, rock debris and volcanic ash) in the acid fluid. In addition to the formation of intragranular dissolution pores of feldspar and rock debris, the edges of unstable components were largely dissolved. Thus, intergranular dissolution was formed (Figs. 3(g), 3(h), and 3(i)). In conclusion, all the samples were dominated by residual intergranular pores, but the specific surface area of Types C and B was much higher than that of Type A.

Figure 4 shows that the characteristics of mercury injection and removal curves of the three types of samples were significantly different. Figure 4(a) shows that the mercury volume of Type A was close to 0 at an injection

pressure of less than 1 MPa, indicating that pores with a diameter larger than 10000 nm were not developed in those samples. Such samples mainly developed pores in the range of 100−5000 nm, and the developed pores around 1000 nm were the most. The pore distribution morphology of Type A was unimodal. Figure 4(c) shows that the mercury volume of Type B was close to 0 at an injection pressure of less than 1 MPa, indicating that pores with a diameter larger than 10000 nm were not developed in those samples. Compared with Type A, Type B had much higher mercury saturation. Pores in the range of 100−1000 nm were mainly developed in such samples, and the developed pores around 1000 and4000nm were the most. The pore distribution morphology of Type A was bimodal (Fig. 4(d)). Figure 4(e) shows that the mercury volume of Type C was close to 0 at an injection pressure of less than 0.1 MPa, indicating that pores with a diameter larger than 100000 nm were
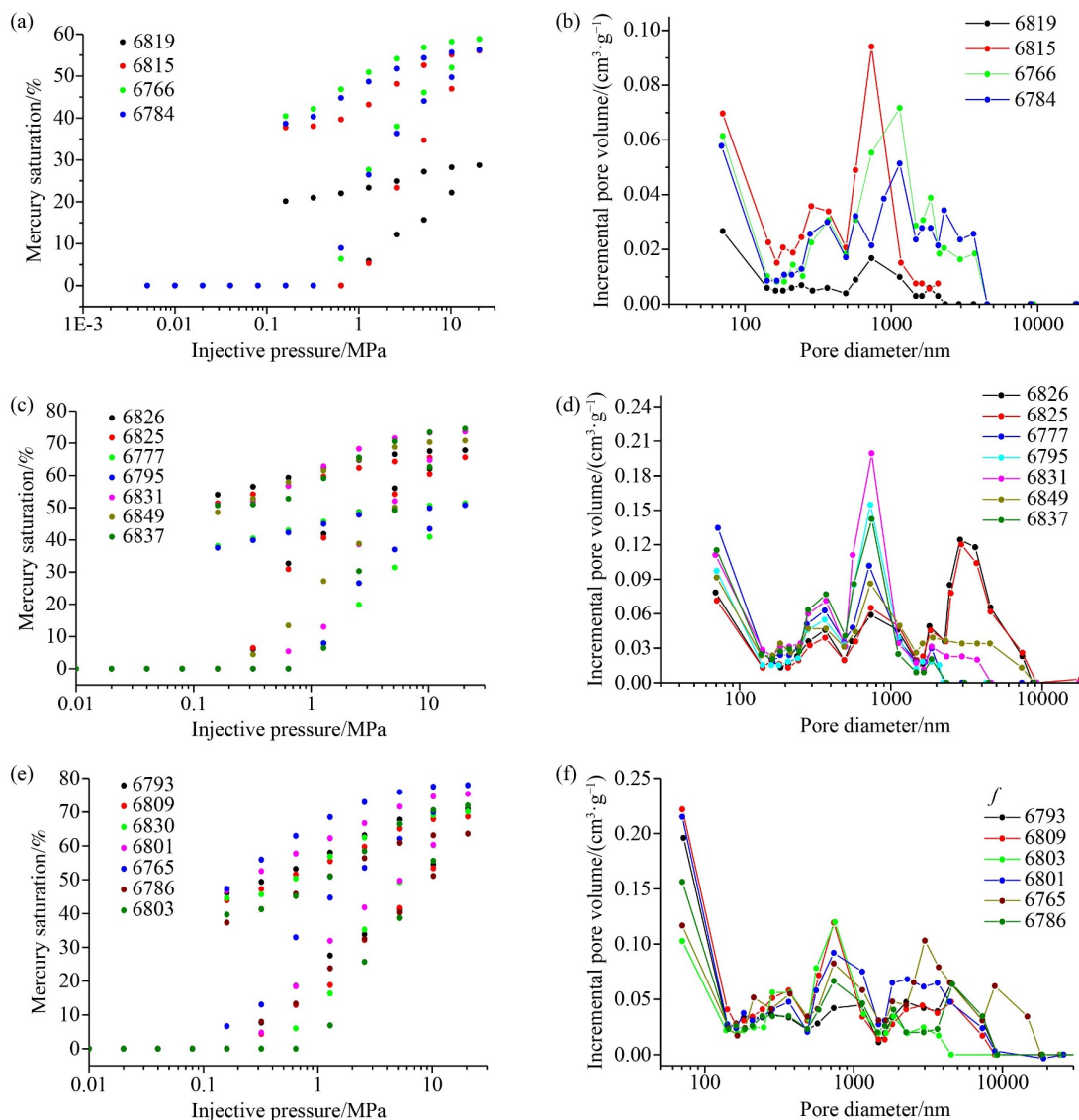
Fig. 4 Mercury intrusive and removal curve of different types of samples and pore diameter distribution using HPMI tests.

not developed in those samples. Compared with Types A and B, Type C had the largest mercury saturation. The pore distribution morphology of Type A was trimodal (Fig. 4(f)).

Figure 5 shows that Type C had the largest total pore volume, followed by Types B and A. The reason is that pores of Types A and B all belong to inter-granular residual pores. The results of pore volume percentage show that the difference in the development of pores with diameters smaller than 200 nm was more significant in different types of samples.

3.2 Pore diameter distribution heterogeneity using different fractal dimension models

The fractal dimension D_M using the Menger model (Eq. (1)) is shown in Fig. 6. Figures 6(a), 6(b), and 6(c) show that the overall fractal curve can be fitted to a straight line, with R^2 over 0.8. Many studies have concluded that the line segment using the Menger model can be divided into two segments, which was inconsistent with Fig. 6. The reason is that only pores with a diameter of 200−10,000 nm were studied in this paper, and pores with a diameter less than 100 nm were not developed. Figure 6(d) indicates that D value of Type C was lower than that of Types A and B, indicating that PSD heterogeneity of Type C was weaker. It is related to the fact that the pore distribution of Type C was trimodal, and the pore size range of different pores was evenly distributed (Fig. 4(f)).

The fractal dimension D_S using the Sierpinski model (Eq. (2)) is shown in Fig. 7. Figures 7(a), 7(b), and 7(c) show that the overall fractal curve can be fitted to a straight line, with a R^2 over 0.75. The fitting degree of line segment fitted by the Sierpinski model was significantly lower than that of the Merger model, indicating that the Merger model was more applicable to characterizing PSD heterogeneity of sandstone samples. Figure 7(d) shows that D values of different types of samples were less different, and it was related to the lower fit of the linear formula.

The fractal dimension D_T using the thermodynamic model (Eq. (3)) is shown in Fig. 8. Figures 8(a), 8(b), and 8(c) show that the overall fractal curve can be fitted to a straight line, with a R^2 over 0.95. The linear fitting of this model was much better than those of the Menger model and the Sierpinski model. Figures 8(a), 8(b), and 8(c) show that the pore distribution of all the samples had fractal characteristics. Many studies have concluded that the line segment using the thermodynamic model can be regarded as straight lines, which was consistent with Fig. 8. Figure 8(d) indicates that D value of Type C was higher than that of Types A and B, indicating that PSD heterogeneity of type C was stronger. It is related to the fact that the pore volume of Type C was larger than Types A and B (Fig. 4).

Using the mercury intrusive curve of a representative sample 6761, a double logarithmic plot of the partition function $x (q, \varepsilon)$ and the scale size ε was studied (Fig. 9).
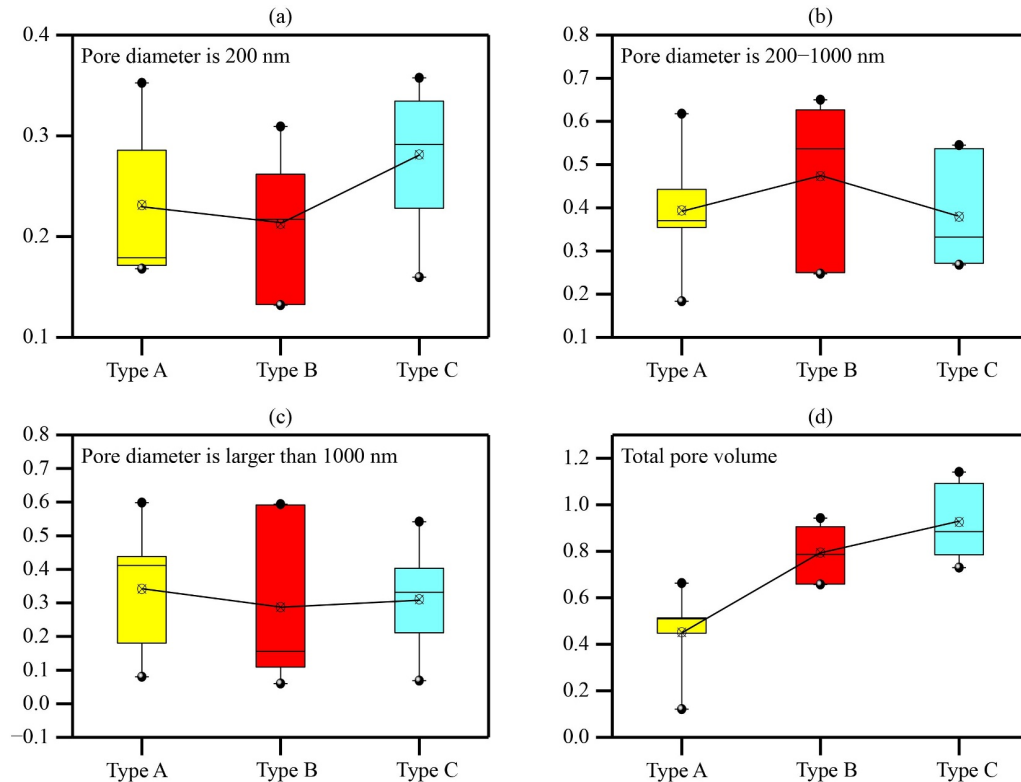

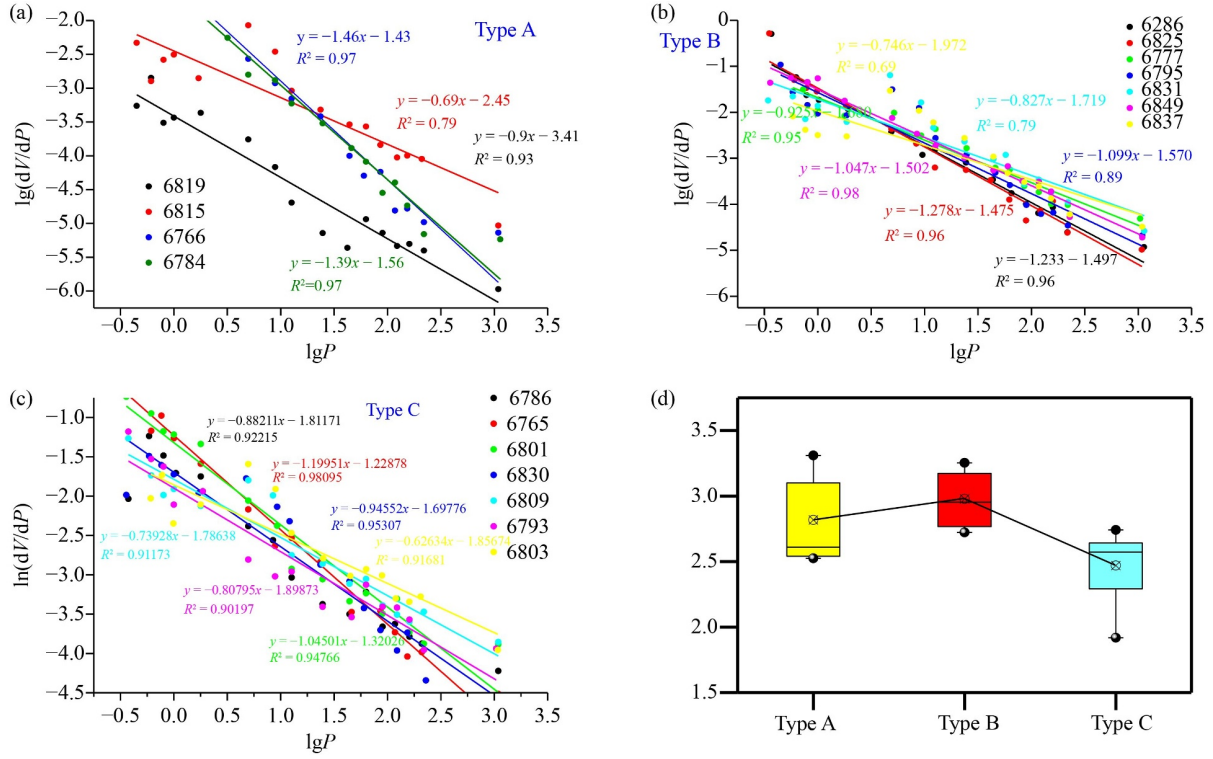**Fig. 5** Comparison of incremental pore volume in different types of samples.

Fig. 6 Fractal dimension of different types of samples using the Menger model.
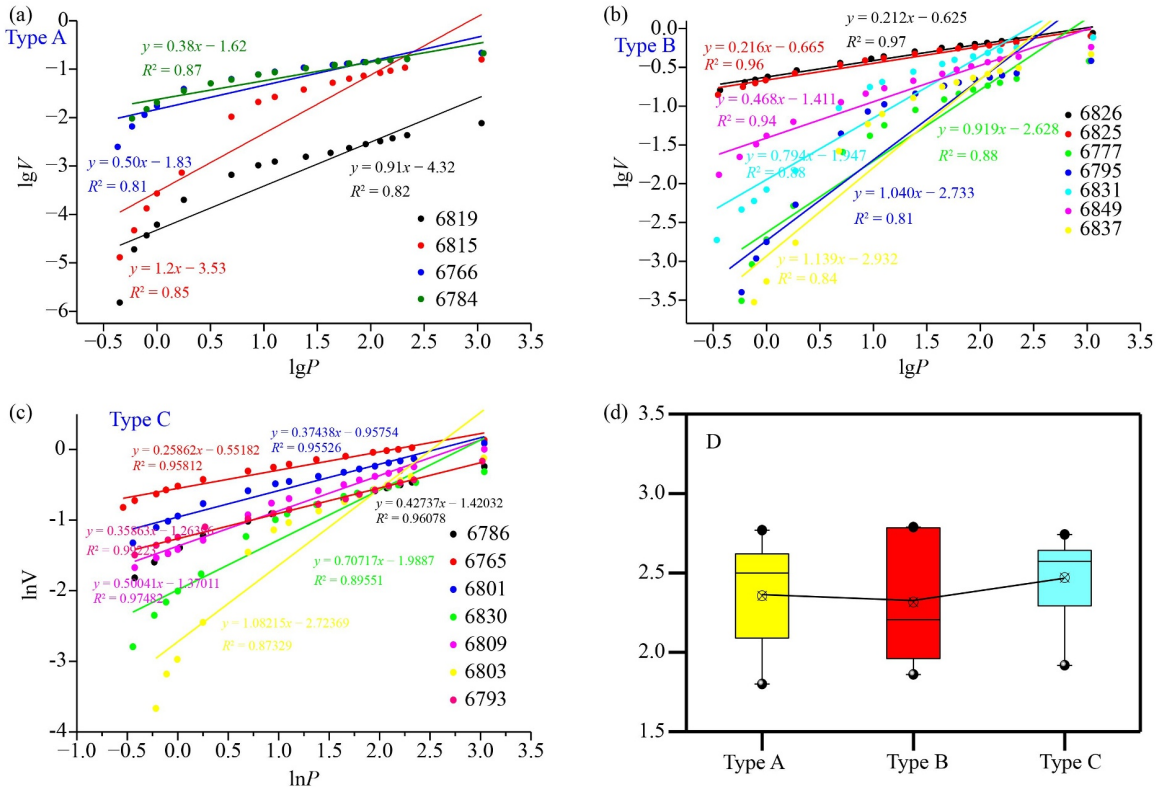

Fig. 7 Fractal dimension of different types of samples using the Sierpinski model.

Figure 9(a) shows that lg[u_i (q,ε)] and lg(ε) exhibited a clear linear relationship, indicating that the PSD of pores had multiple fractal behavior. at $q < 0$, there was a negative correlation between lg[u_i (q,ε)] and lg(ε), whilst they had a positive correlation at $q > 0$. This indicates that the quality index function varied from
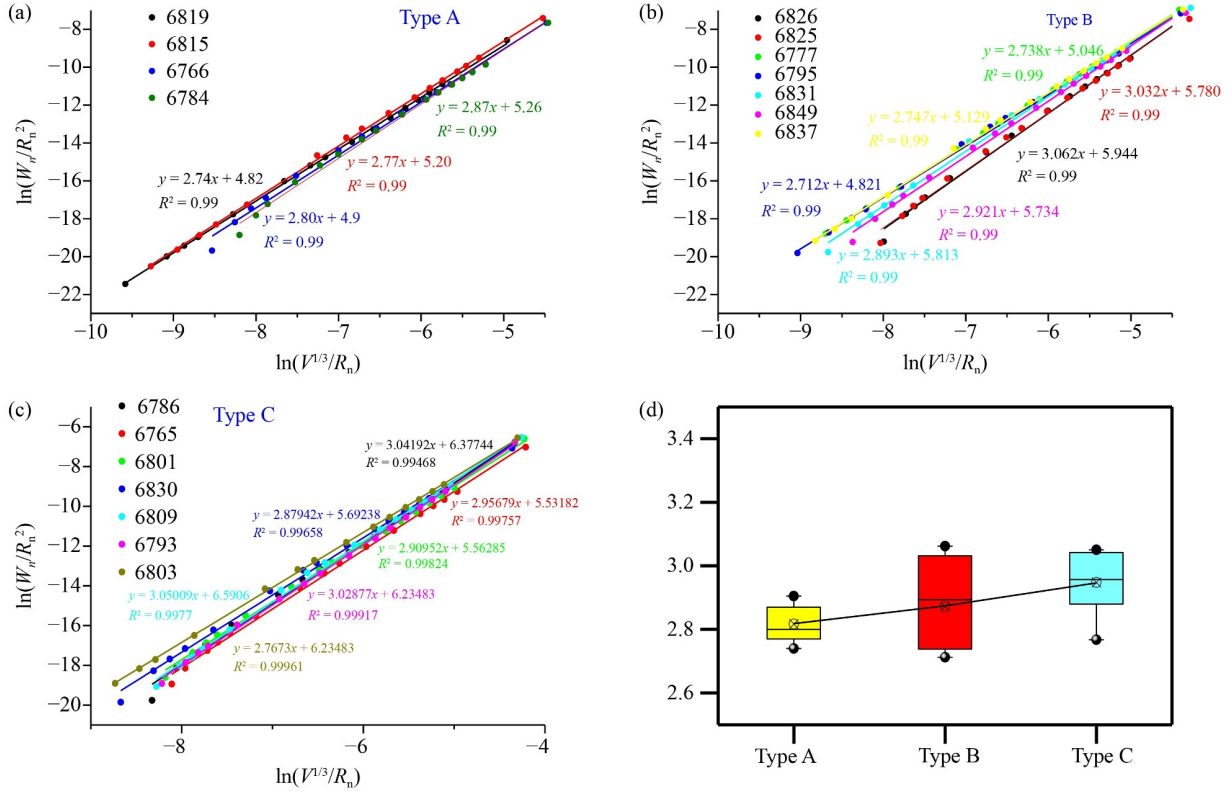
Fig. 8 Fractal dimension of different types of samples using the thermodynamic model.
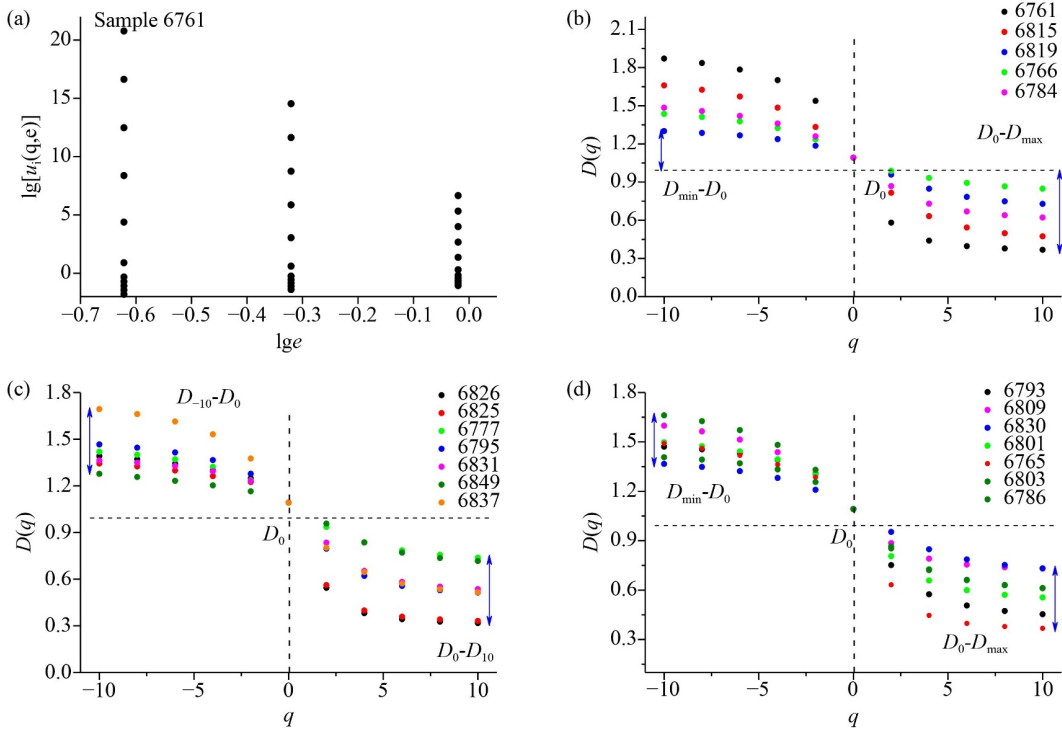

Fig. 9 Multi-fractal dimension of pores among different types of samples.

negative to positive as the statistical matrix varied from small to large. In addition, the fitting line gradually varied from sparse to dense, reflecting that the PSD range was small.

Multi-fractal parameters of pores were calculated. Figures 9(b), 9(c), and 9(d) show that q versus $D(q)$ spectra of all samples had a distinct reverse-shaped curve, further confirming that the PSD was multi-fractal. This

spectral curve can characterize the PSD complexity at different q. For one sample, there was little difference between D_{-10}–D_0 and D_0–D_{10}, indicating that the pore size range of different pores was evenly distributed.

It can be seen that D_{10} of Type A samples was larger than that of Types B and C samples, indicating that Type A samples had stronger distribution heterogeneity in the lowest-value area of the pore volume. D_{-10} of Type A samples was larger than that of Types B and C samples, indicating that Type A had stronger distribution heterogeneity in the largest-value area of the pore volume. Then, D_{-10}–D_{10} of Type A samples was larger than that of Types *B* and *C* samples, indicating that PSD heterogeneity of Type B was stronger.

Figure 10(a) shows that there was no clear linear relationship between the fractal dimension values using the Sierpinski model and between those using the Menger model. However, there was a significant negative linear relationship between D_M and D_S in Type A samples.

Then, there was no clear linear relationship between D_M and D_S in Types B and C samples. There was no obvious linear relationship between the fractal dimension values using the S model and between those using the thermodynamic model. However, there was a significant negative linear relationship between D_T and D_S in Types A and B samples. Then, there was no clear linear relationship between D_M and D_S in the Type C samples (Fig. 10(b)). Different from Figs. 10(a) and 10(b), there was also no linear relationship between the fractal dimension values using the thermodynamic model and between those using the Menger model, and there was no obvious linear relationship between D_M and D_T in different types of samples (Fig. 10(c)). It indicates that different single fractal models had clear differences in characterizing PSD heterogeneity of those samples. Figures 10(d), and 10(e) show that there was a linear positive correlation between D_{-10}–D_{10} and D_0–D_{10}, indicating that the high-value area of pore volume
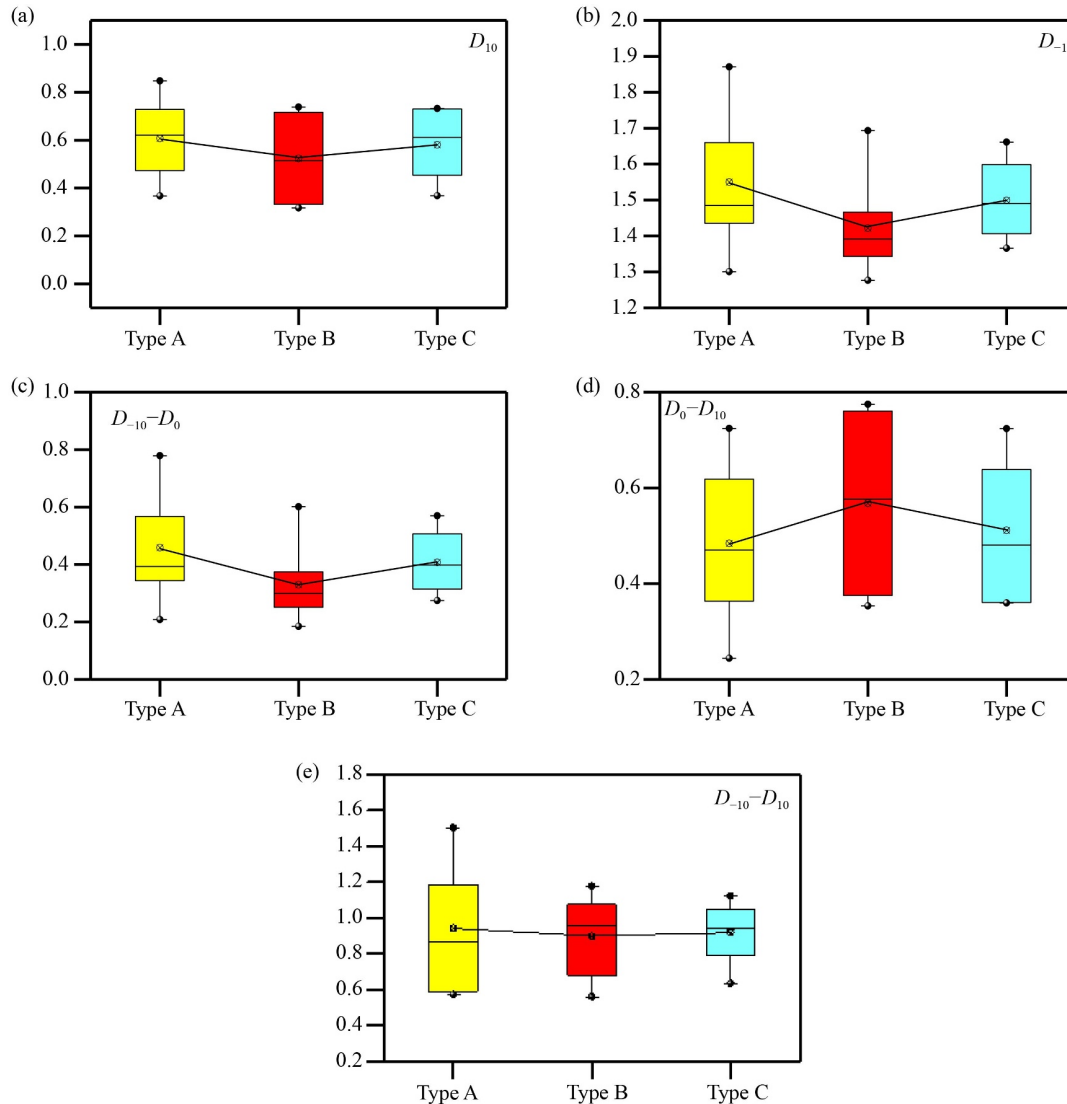

Fig. 10 Comparison of multifractal characteristics among different types of samples.

distribution determines the overall heterogeneity of pore distribution (Fig. 11).

Figure 12(a) shows that there was no correlation between total pore volume and each single fractal dimension. Figure 12(b) indicates that there was no correlation between total pore volume and each single fractal dimension. D_M increased linearly with the development of pores less than 200 nm, indicating that PSD heterogeneity increased gradually. However, there was no correlation between pore volume of pore with a diameter lower than 200 nm and D_S and D_T. It indicates that pores smaller than 200 nm were not the key pores affecting PSD heterogeneity. Compared with smaller pore size, the pore volume of pores with a diameter of 200−1000 nm and above 1000 nm had a linear relationship with those single fractal parameters.

3.3 Effects of confining pressure on permeability variation

Figure 13 shows that the initial permeability of the three type sample varied significantly, and the seepage pore and micro fractures of Type C samples of medium rank coal were relatively developed. Thus, the permeability and porosity of Type C was generally greater than that of Types A and B. When the effective stress increased from 0 to 50 MPa, the permeability of all samples decreased exponentially, and the R^2 was 0.90−0.99. In addition, with the increase of effective stress, the permeability of the sample varied in stages. Specifically, permeability decreased rapidly with the increase of confining pressure at an effective stress less than 10 MPa, and the average decline of each sample can reach 86%. However, at an effective stress greater than 10 MPa, the permeability
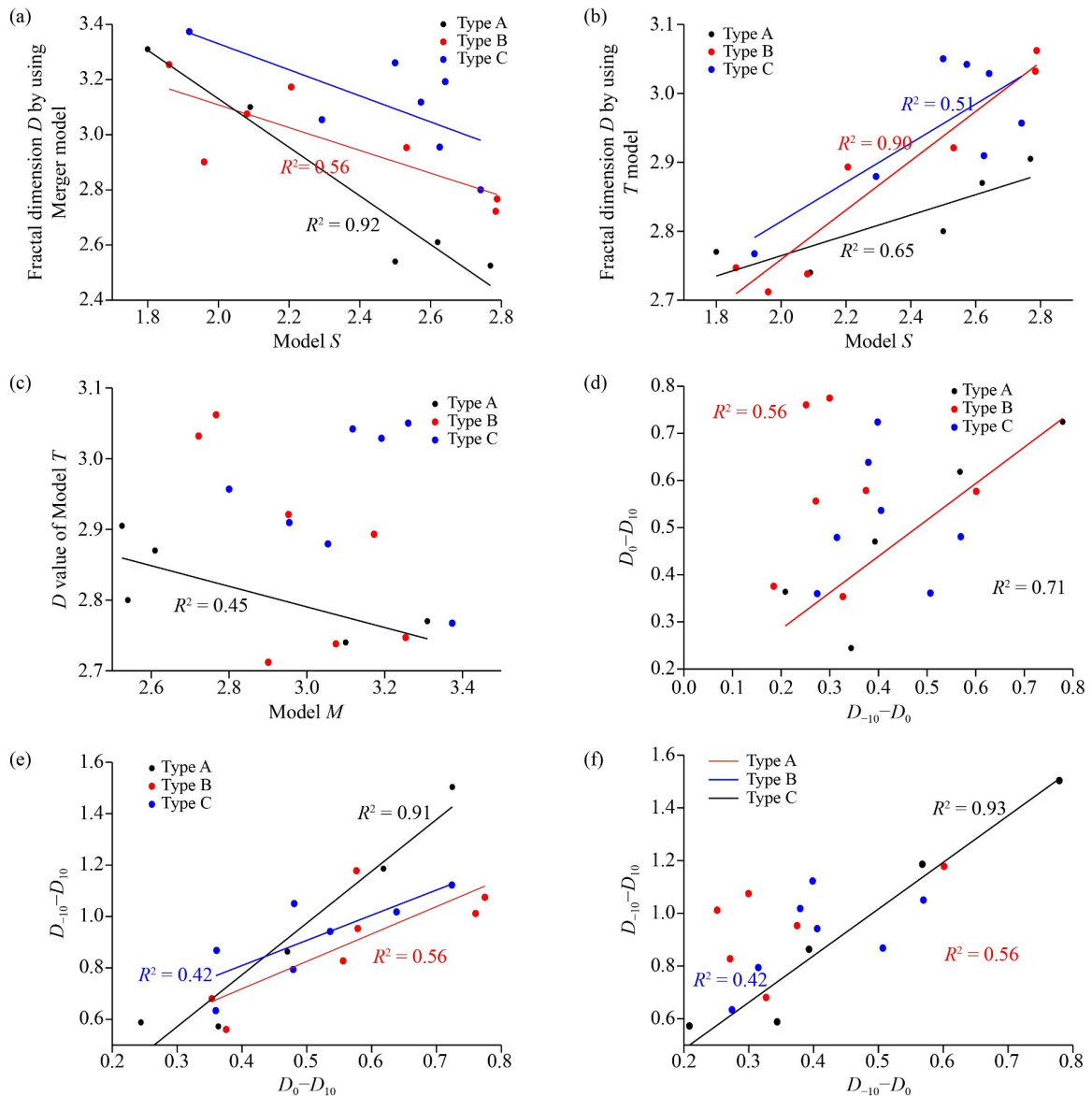

Fig. 11 Relationship between fractal dimension values using different fractal models.
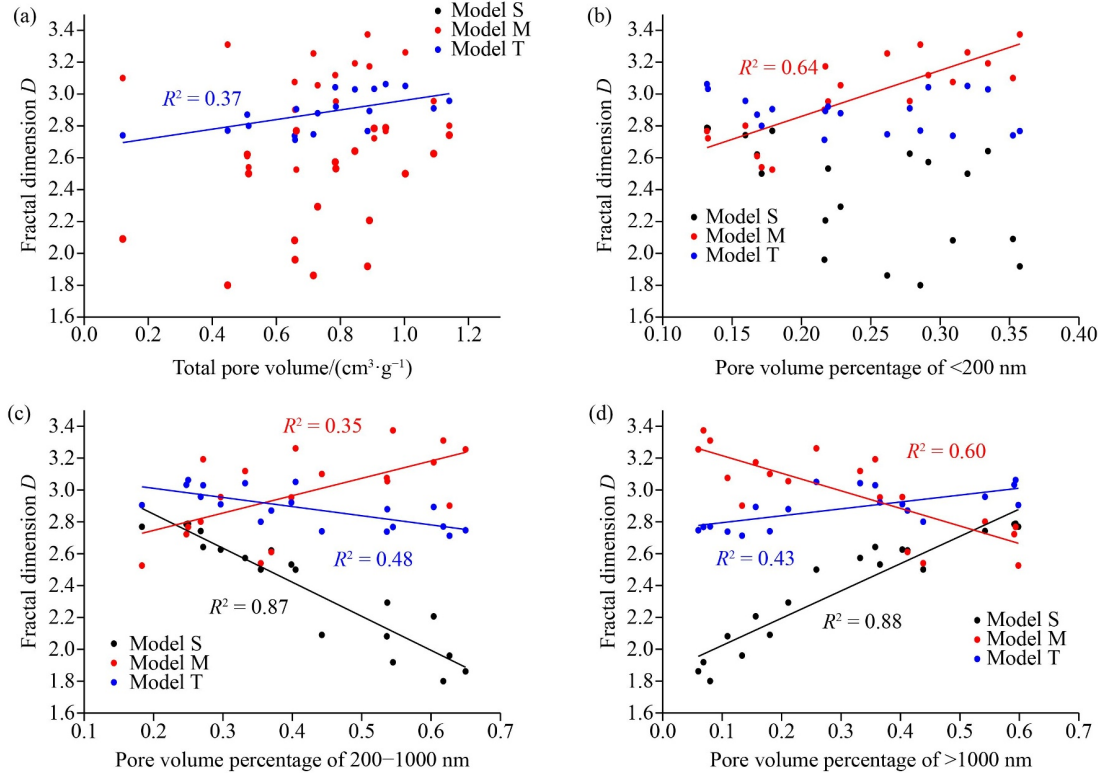
Fig. 12 Relationship between pore volume at different stages and different fractal dimensions.

declined slowly and tended to be stable. The analysis shows that the volume of pores and fractures in the sample at the initial stage of stress action was not compressed. The highly compressible space in seepage pore and fractures was large, resulting in a clear decline of coal sample permeability at this stage. With the increase of stress, compressible space for pore volume such as macro-pores continuously decreased, mainly compressed by pore volume such as adsorption pores. The compressibility coefficient decreased, resulting in the relatively stable change of sample permeability at this stage.

Figure 14 shows that the porosity and permeability variation rate of all the samples was 0.86−0.95 and 0.1−0.8, respectively. The permeability and porosity of Type C sample 13 was the most sensitive to pressure, and the porosity and permeability variation rate can reach 0.86 and 0.2, respectively. Section 3.1 shows that larger pores were developed in Sample 13, with large initial permeability. With the continuous increase of effective stress, the compressible space provided by the larger pore was fully compressed, resulting in the highest permeability variation rate. The fracture of Sample was not developed, resulting in that the compressible space in the high-stress stage is mainly provided by micro-pores. Larger pores affecting permeability showed smaller variations. Thus, the permeability variation rate was relatively small.

The compressibility of typical samples is calculated using Eq. (8), and the calculation results are shown in Fig. 15. There was a clear linear relationship between $-\ln(k/k_0)/3$ of different samples and the effective stress P. The average compression coefficient of the fracture can be obtained using the slope. The compressibility of all samples ranged between 0.002−0.02 MPa^{-1}. Based on the compressibility, all samples can be divided into two categories. One is represented by Samples 5 and 13, with the compressibility of about 0.02 and 0.01 MPa^{-1}. The other one is represented by the remaining samples, with the compressibility of only 0.002 and 0.008 MPa^{-1}, which was mainly related to the underdevelopment of micro-fracture in the corresponding samples.

3.4 Main controlling factors affecting porosity and permeability

Figure 16(a) shows that there was a power function relationship between compressibility and permeability variation rate, with a R^2 of 0.93. The influence of pore volume parameters (e.g., total pore volume) on the compressibility coefficient was weak (Fig. 16(b)). D_M increased linearly with the increase of compressibility, and there was no clear relationship between other single fractal dimensions and compressibility (Fig. 16(c)). It indicates that the fractal dimension from the Merger model was the key factor affecting the compressibility. Figure 15(d) shows that compressibility increased with the increase of quartz and feldspar content. The micro-
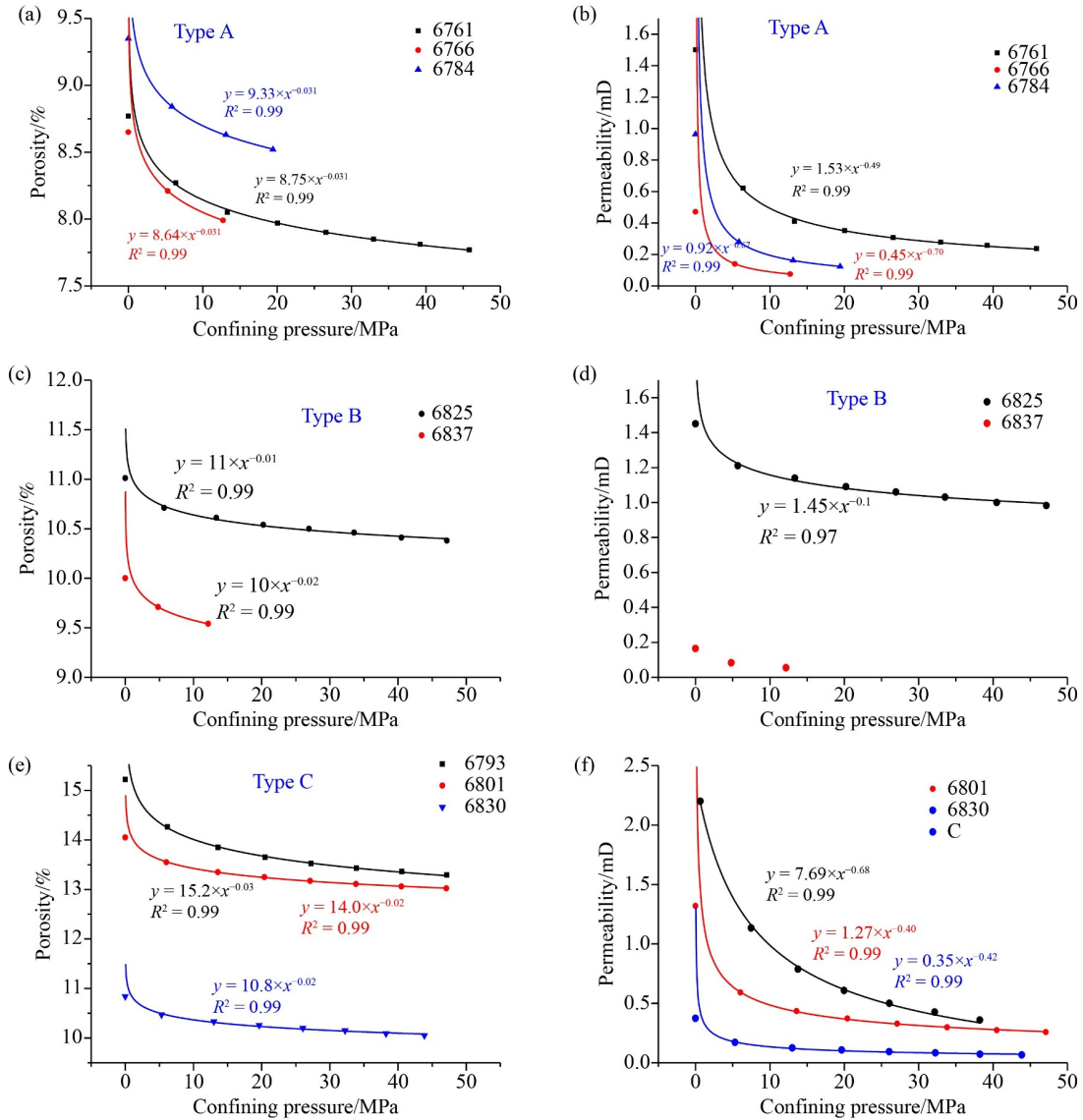
Fig. 13 Permeability and porosity variation of typical samples with confining pressure.

fracture developed more with higher content of quartz and feldspar, resulting in the larger pore compression space under the effect of confining pressures.

Most of the studies have been focused on the maximum permeability variation rate. Figure 16(a) shows that there was a positive linear relationship between porosity variation rate at a pressure of 20 MPa and porosity variation rate at a pressure of 50 MPa, with a R^2 of 0.98. There was no clear correlation between pore structure parameters, mineral component content and porosity variation rate. Gao (2016) showed that multi-fractal dimension, $D_{-10}-D_0$ and $D_{-10}-D_{10}$ had a positive linear correlation with permeability variation rate, indicating that stronger pore heterogeneity induced higher damaging effects of confining stress on permeability. This phenomenon is not consistent with the conclusions in Figs. 16(c) and 16(d). All samples belong to a sandstone reservoir with large initial porosity and permeability. The

pore structure parameters calculated in this paper only involved pores smaller than 10000 nm, and the micro-fracture was not considered in the statistics of HPMI data. When the overburden porosity and permeability test was carried out, the micro-fracture of the cylinder samples was relatively developed. Thus, the correlation between the pore structure parameters, porosity and permeability variation rate and compressibility coefficient was lower (Fig. 17).

4   Conclusions

In this paper, 18 sandstone samples were collected from the study area for HPMI tests, mineral composition and thin-slicing analysis. The fractal dimension of the pore volume was calculated using the Sierpinski model, the Menger model, thermodynamic model and the multi-
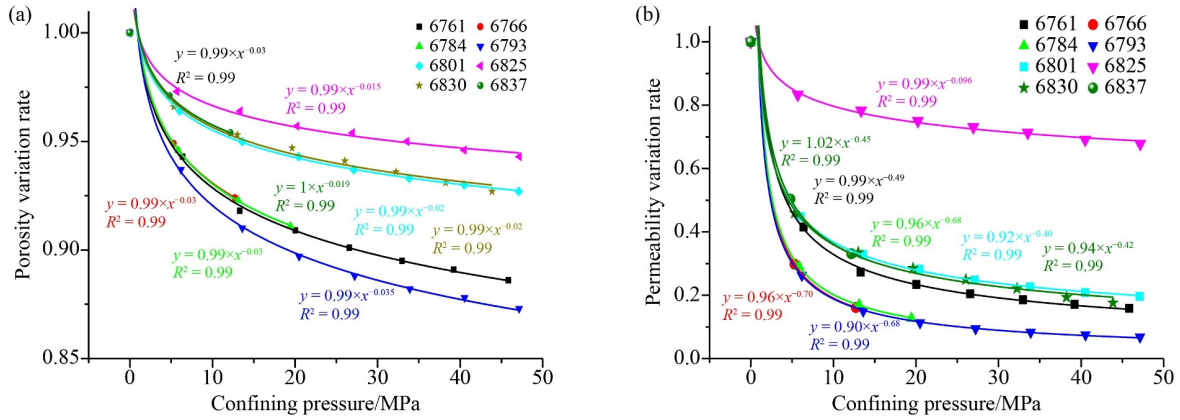
Fig. 14 Permeability and porosity variation rate of typical samples.
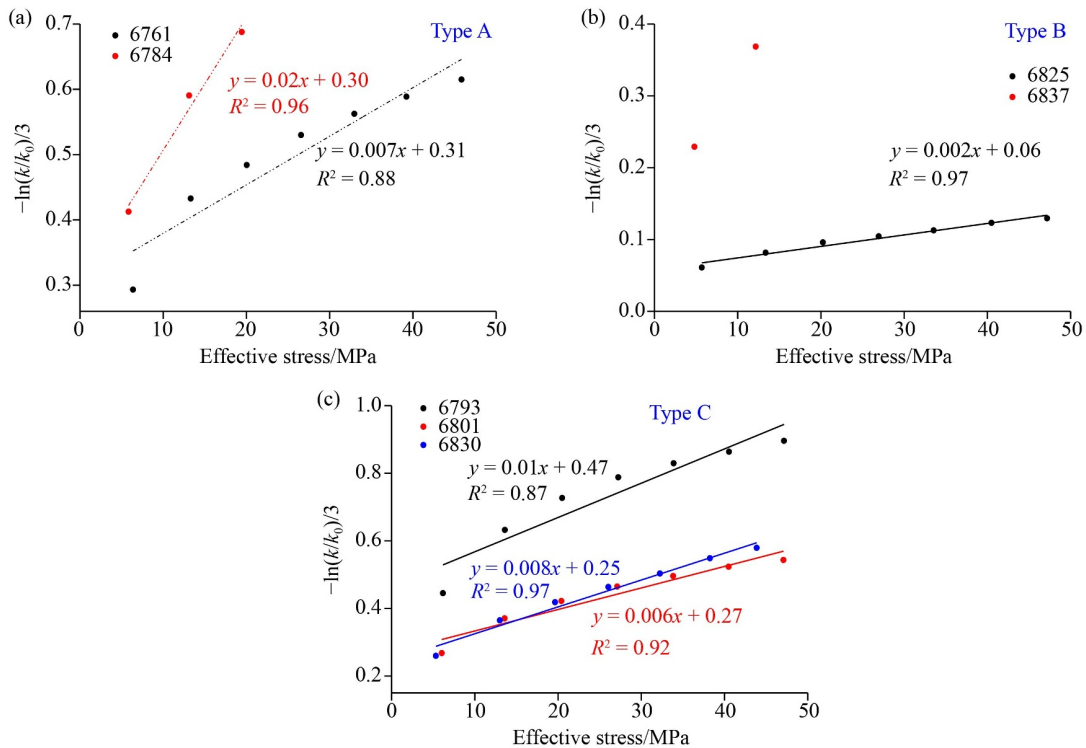

Fig. 15 Different sample's compressibility using permeability variation.

fractal model, respectively. The effect of the confining pressure on the porosity and permeability variation was studied. The relationship between fractal dimension and porosity/permeability variation rate, and pore compressibility were studied. The conclusions are as follows.

1) All sandstone samples were classified into three types, i.e., Type A, lower total injection volume and lower mercury removal efficiency; Type B, higher total injection volume and lower mercury removal efficiency; Type C, higher total injection volume and higher mercury removal efficiency.

2) Four fractal models had poor applicability in characterizing fractal characteristics of different sample types. The fractal dimension from the Sierpinski model had a good linear correlation with D calculated by other

models. Pores with lower volume dominated the overall pore distribution heterogeneity by multi-fractal dimension. The pore diameter lying within 200−1000 nm and larger than 1000 nm were the key pore size interval to determine the fractal characteristics.

3) With the increase of the confining pressure, porosity and permeability both decreased in the form of the power function. The compressibility coefficient of typical samples was 0.002−0.2 MPa^{-1}. The compressibility of Types A and B was significantly higher than that of Type C, indicating that the total pore volume was not the key factor affecting the pore compressibility.

4) Compared with unconventional reservoirs (coal and shale), sandstone with higher initial permeability and porosity had weaker correlations between pore structure
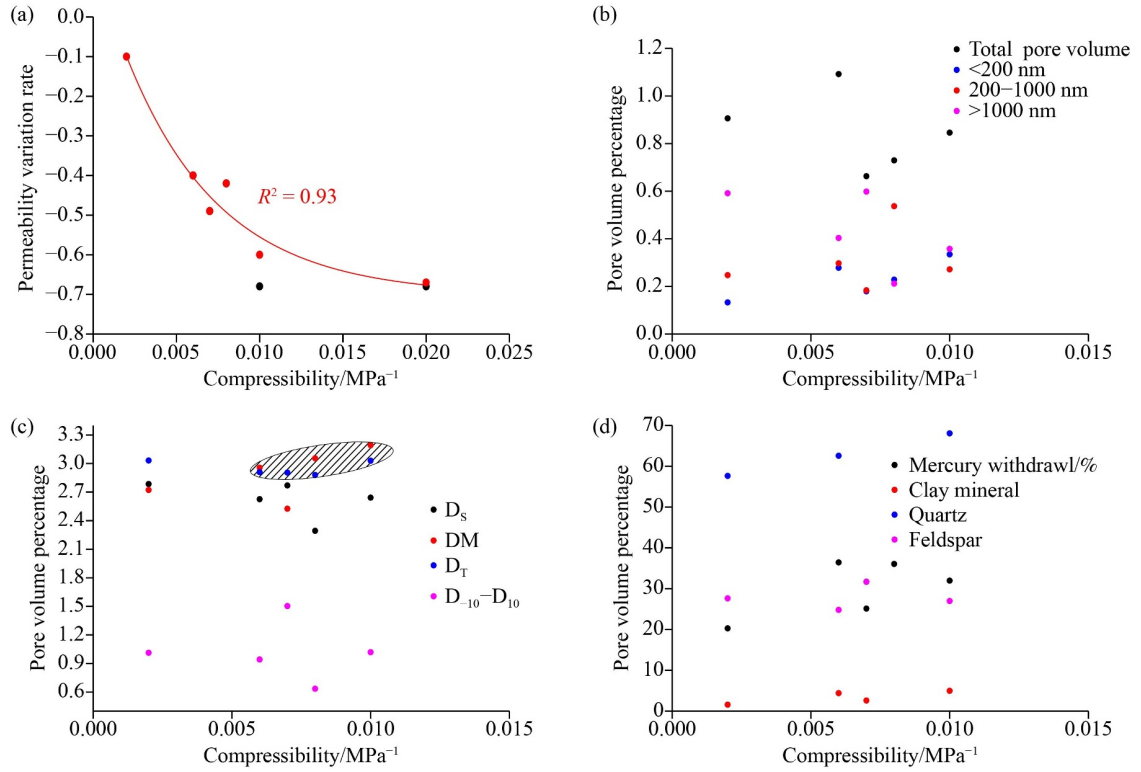
Fig. 16 Correlation between compressibility and pore volume, fractal dimension and mineral composition.
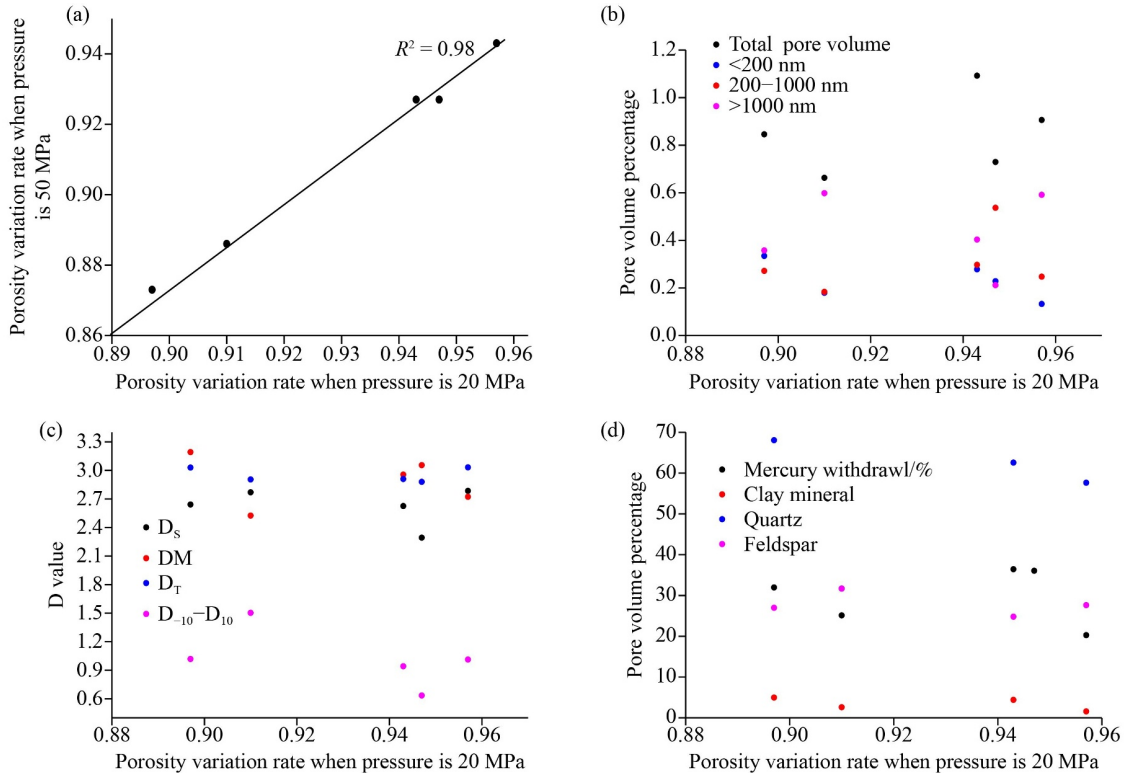

Fig. 17 Correlation between porosity variation rate and pore volume, fractal dimension and mineral composition.

parameters and compressibility. This is mainly related to the size range of the pores characterized by high-pressure mercury intrusion data.

University of Mining and Technology) (No. 2023-007) and Shandong Coalfield Geological Bureau Research Special Project of 2024s (No. MTDZKY-2024-35).

Competing interests   The authors declare that they have no competing interests.

References

Angulo R, Alvarado V, Gonzalez H (1992). Fractal dimensions from mercury intrusion capillary tests. In: SPE Latin America Petroleum Engineering Conference. Society of Petroleum Engineers

Cai Y, Li Q, Liu D, Zhou Y, Lv D (2018). Insights into matrix compressibility of coals by mercury intrusion porosimetry and N_2 adsorption. Int J Coal Geol, 200: 199–212

Cai Y, Liu D, Pan Z, Che Y, Liu Z (2016). Investigating the effects of seepage-pores and fractures on coal permeability by fractal analysis. Transp Porous Media, 111(2): 479–497

Cai Y, Liu D, Yao Y, Li J, Liu J (2011). Fractal characteristics of coal pores based on classic geometry and thermodynamics models. Acta Geol Sin Engl Ed, 85(5): 1150–1162

Friesen W I, Mikula R J (1987). Fractal dimensions of coal particles. J Colloid Interface Sci, 120(1): 263–271

Gao L (2016). Sedimentary Reservoir Study of Permian Shang Wuerhe Formation in Well Block Jinlong-2 of Junggar Basin. Dissertation for Master's Degree. Qingdao: China University of Petroleum

He H, Li S, Liu C, Kong C, Jiang Q, Chang T (2020). Characteristics and quantitative evaluation of volcanic effective reservoirs: a case study from Junggar Basin, China. J Petrol Sci Eng, 195: 107723

Hou X, Zhu Y, Chen S, Wang Y, Liu Y (2020). Investigation on pore structure and multifractal of tight sandstone reservoirs in coal bearing strata using LF-NMR measurements. J Petrol Sci Eng, 187: 106757

Hu Y, Guo Y, Zhang J, Shangguan J, Li M, Quan F, Li G (2020). A method to determine nuclear magnetic resonance T_2 cutoff value of tight sandstone reservoir based on multifractal analysis. Energy Sci Eng, 8(4): 1135–1148

Lai J, Wang G, Fan Z, Chen J, Wang S, Zhou Z, Fan X (2016). Insight into the pore structure of tight sandstones using NMR and HPMI measurements. Energy Fuels, 30(12): 10200–10214

Lai J, Wang G, Wang Z, Chen J, Pang X, Wang S, Zhou Z, He Z, Qin Z, Fan X (2018). A review on pore structure characterization in tight sandstones. Earth Sci Rev, 177: 436–457

Li J, Wang S, Lu S, Zhang P, Cai J, Zhao J, Li W (2019). Micro-distribution and mobility of water in gas shale: a theoretical and experimental study. Mar Pet Geol, 102: 496–507

Li K (2010). Analytical derivation of Brooks-Corey type capillary pressure models using fractal geometry and evaluation of rock heterogeneity. J Petrol Sci Eng, 73(1−2): 20–26

Li W, Liu H, Song X (2015). Multifractal analysis of Hg pore size distributions of tectonically deformed coals. Int J Coal Geol, 144–145: 138–152

Liu G, Meng Z, Luo D, Wang J, Gu D, Yang D (2020). Experimental evaluation of interlayer interference during commingled production in a tight sandstone gas reservoir with multi-pressure systems. Fuel, 262: 116557

Liu K, Ostadhassan M, Kong L (2019). Fractal and multifractal characteristics of pore throats in the Bakken shale. Transp Porous Media, 126(3): 579–598

Lu G, Wang J, Wei C, Song Y, Yan G, Zhang J, Chen G (2018). Pore fractal model applicability and fractal characteristics of seepage and adsorption pores in middle rank tectonic deformed coals from the Huaibei coal field. J Petrol Sci Eng, 171: 808–817

Mastalerz M, Hampton L, Drobniak A, Loope H (2017). Significance of analytical particle size in low-pressure N_2 and CO_2 adsorption of coal and shale. Int J Coal Geol, 178: 122–131

Paz Ferreiro J, Vidal Vázquez E (2010). Multifractal analysis of Hg pore size distributions in soils with contrasting structural stability. Geoderma, 160(1): 64–73

Peng C, Zou C, Yang Y, Zhang G, Wang W (2017). Fractal analysis of high rank coal from southeast Qinshui basin by using gas adsorption and mercury porosimetry. J Petrol Sci Eng, 156: 235–249

Pfeifer P, Avnir D (1983). Chemistry in noninteger dimensions between two and three. I. Fractal theory of heterogeneous surfaces. J Chem Phys, 79(7): 3558–3565

Qiao J, Zeng J, Chen D, Cai J, Jiang S, Xiao E, Zhang Y, Feng X, Feng S (2022). Permeability estimation of tight sandstone from pore structure characterization. Mar Pet Geol, 135: 105382

Qin L, Zhai C, Liu S, Xu J, Wu S, Dong R (2018). Fractal dimensions of low rank coal subjected to liquid nitrogen freeze-thaw based on nuclear magnetic resonance applied for coalbed methane recovery. Powder Technol, 325: 11–20

Schmitt M, Fernandes C P, Da Cunha Neto J A B, Wolf F G, dos Santos V S S (2013). Characterization of pore systems in seal rocks using nitrogen gas adsorption combined with mercury injection capillary pressure techniques. Mar Pet Geol, 39(1): 138–149

Shao P, Wang X, Song Y, Li Y (2018). Study on the characteristics of matrix compressibility and its influence factors for different rank coals. J Nat Gas Sci Eng, 56: 93–106

Su P, Xia Z, Qu L, Yu W, Wang P, Li D, Kong X (2018). Fractal characteristics of low-permeability gas sandstones based on a new model for mercury intrusion porosimetry. J Nat Gas Sci Eng, 60: 246–255

Wang X, Hou J, Song S, Wang D, Gong L, Ma K, Liu Y, Li Y, Yan L (2018). Combining pressure-controlled porosimetry and rate-controlled porosimetry to investigate the fractal characteristics of full-range pores in tight oil reservoirs. J Petrol Sci Eng, 171: 353–361

Wang Y, Zhu Y, Chen S, Li W (2014). Characteristics of the nanoscale pore structure in northwestern Hunan shale gas reservoirs using field emission scanning electron microscopy, high-pressure mercury intrusion, and gas adsorption. Energy Fuels, 28(2): 945–955

Yao Y, Liu D (2012). Comparison of low-field NMR and mercury intrusion porosimetry in characterizing pore size distributions of coals. Fuel, 95: 152–158

Yao Y, Liu D, Tang D, Tang S, Huang W, Liu Z, Che Y (2009). Fractal characterization of seepage-pores of coals from China: an

investigation on permeability of coals. Comput Geosci, 35(6): 1159–1166

Yu S, Bo J, Pei S, Jiahao W (2018). Matrix compression and multifractal characterization for tectonically deformed coals by Hg porosimetry. Fuel, 211: 661–675

Zhang J, Chu X, Wei C, Zhang P, Zou M, Wang B, Quan F, Ju W (2022). Review on the application of low-field nuclear magnetic resonance technology in coalbed methane production simulation. ACS Omega, 7(30): 25906–26992

Zhang J, Wei C, Chu X, Vandeginste V, Ju W (2020a). Multifractal analysis in characterizing adsorption pore heterogeneity of middle- and high-rank coal reservoirs. ACS Omega, 5(31): 19385–19401

Zhang J, Wei C, Ju W, Yan G, Lu G, Hou X, Kai Z (2019a). Stress sensitivity characterization and heterogeneous variation of the pore-fracture system in middle-high rank coals reservoir based on NMR experiments. Fuel, 238: 331–344

Zhang J, Wei C, Zhao J, Ju W, Chen Y, Tamehe L S (2019b).

Comparative evaluation of the compressibility of middle and high rank coals by different experimental methods. Fuel, 245: 39–51

Zhang P, Lu S, Li J, Chang X (2020b). 1D and 2D Nuclear magnetic resonance (NMR) relaxation behaviors of protons in clay, kerogen and oil-bearing shale rocks. Mar Pet Geol, 114: 104210

Zhu S, Du Z, Li C, Salmachi A, Peng X L, Wang C W, Yue P, Deng P (2018). A semi-analytical model for pressure-dependent permeability of tight sandstone reservoirs. Transp Porous Media, 122(2): 235–252

Zou C, Zhu R, Liu K, Su L, Bai B, Zhang X, Yuan X, Wang J (2012). Tight gas sandstone reservoirs in China: characteristics and recognition criteria. J Petrol Sci Eng, 88–89: 82–91

Zou M, Wei C, Zhang M, Shen J, Chen Y, Qi Y (2013). Classifying coal pores and estimating reservoir parameters by nuclear magnetic resonance and mercury intrusion porosimetry. Energy Fuels, 27(7): 3699–3708